Journal of Luminescence 190 (2017) 234–241

Contents lists available at ScienceDirect

Journal of Luminescence

journal homepage: www.elsevier.com/locate/jlumin

On the influence of calcium substitution to the optical properties of Cr^{3+} doped $SrSc_2O_4$

Beata Malysa[a,b,*], Andries Meijerink[b,**], Weiwei Wu[b], Thomas Jüstel[a]

[a] Münster University of Applied Sciences, Stegerwaldstrasse 39, D-48565 Steinfurt, Germany
[b] University Utrecht, Princetonplein 1, NL-3584 Utrecht, The Netherlands

ARTICLE INFO

Keywords:
Cr^{3+} photoluminescence
Scandates
Near infrared emitting phosphors
Racah parameters
Fano resonance
Crystal field splitting
3*d* – 3*d* emission

ABSTRACT

Cr^{3+} doped (Sr,Ca)Sc_2O_4 samples were synthesized and investigated in view of their potential application as luminescent converters for high power broad band near infrared (NIR) sources. The synthesis of the Cr^{3+} activated MSc_2O_4 (M = Ca, Sr) samples was performed by solid state reactions. Obtained powders show broad band near infrared emission between 700 and 1000 nm under excitation in the blue spectral range. The emission is assigned to the intraconfigurational ($3d^3$) $^4T_2 \rightarrow {}^4A_2$ transition on Cr^{3+}. As the calcium concentration in $SrSc_2O_4$ was increased, a blue shift of the emission spectra was observed. In order to gain insight in the luminescence properties, the crystal field strength, Racah parameters and phonon coupling parameters were examined. Additionally, the influence of temperature in the range between 4 and 500 K on the photoluminescence of the $CaSc_2O_4$:Cr^{3+} and $SrSc_2O_4$:Cr^{3+} was investigated. At 4 K a µs decay time typical of Cr^{3+} broad band d-d emission was observed. Between 70 and 350 K the decay time and emission intensity decrease due to thermal quenching. The large Stokes shift of the Cr^{3+} emission (~3000 cm^{-1}) combined with the low energy position of the $^4T_2$ excited state causes non-radiative relaxation to the ground state, already below room temperature. The low thermal quenching temperature of broad band NIR emission is a general problem and the present results provide insight in factors determining thermal quenching.

1. Introduction

The transition metal ion Cr^{3+} is widely applied in solid state laser gain materials, as a co-dopant for persistent phosphors emitting in the near infrared region, and as the optical centre in thermographic phosphors for optical sensing [1–6]. Cr^{3+} doped luminophores are also considered as near infrared (NIR) emitting materials for in-vivo optical imaging due to the rather high penetration depth of NIR radiation into biological tissue [7,8]. Moreover, Cr^{3+} phosphors have a potential application as luminescent converters for near-infrared phosphor-converted light emitting diodes (pc-LED) [9,10].

NIR light sources have a broad area of application in optical communication, environmental monitoring, biomedical imaging, spectroscopy, phototherapy and thermography [11–16]. Commonly used NIR emitters are incandescent bulbs, halogen lamps, silicon carbide heating elements (broad band) and near-infrared GaAs or (Al,Ga)As LEDs (narrow band). However, the application of these NIR sources is hampered by low efficiency, size and (for NIR LEDs) their poor thermal stability, sensitivity towards humidity, and rather low electroluminescence efficiency [17]. A possibility to overcome these obstacles is the use of LEDs based on a blue or near UV emitting (In,Ga)N semiconductor chip in combination with a suitable broad band NIR emitting phosphor. The (In,Ga)N diodes have excellent thermal stability, show extremely high wall-plug efficiency and exhibit very little spectral shift with drive or temperature shift. The temperature of high-power (In,Ga)N LEDs can reach temperatures up to 450 K, which means that the on-chip radiation converter (phosphor) should not suffer from thermal quenching up to this temperature [18].

Cr^{3+} ion has the [Ar]$3d^3$ configuration and its energy level scheme shows an attractive combination of quartet and doublet states. The luminescence of Cr^{3+} doped materials is driven by the energy separation between the low-lying ^2E and $^4T_2$ excited states from the $^4A_2$ ground state. In a strong crystal field, the lowest excited state is ^2E which is identified with a narrow line emission arising from the $^2E \rightarrow {}^4A_2$ transition. In a weak crystal field, the $^4T_2$ excited state lies below ^2E excited states and yields a longer wavelengths broad band emission due to the transition to the $^4A_2$ ground state. The strong dependence of the Cr^{3+} luminescence on the crystal field strength allows us to choose a suitable host material to obtain an emission in a desirable wavelength range. By modifying the crystal field strength of the host material, the

* Corresponding author at: Münster University of Applied Sciences, Stegerwaldstrasse 39, D-48565 Steinfurt, Germany.
** Corresponding author.
E-mail addresses: beata.malysa@fh-muenster.de (B. Malysa), a.meijerink@uu.nl (A. Meijerink), w.wu3@uu.nl (W. Wu), tj@fh-muenster.de (T. Jüstel).

http://dx.doi.org/10.1016/j.jlumin.2017.05.030
Received 5 April 2017; Received in revised form 10 May 2017; Accepted 12 May 2017
Available online 13 May 2017
0022-2313/

emission wavelength from Cr^{3+} can be adjusted. For instance, in Al_2O_3:Cr [19], $BaAl_2O_4$:Cr [20] $Gd_3Ga_5O_{12}$:Cr [21], $LaSc_3(BO_3)_4$:Cr [22], $ZnWO_4$:Cr [23] the emission maxima are at 694 nm (R-line), 705 nm, 730 nm, 963 nm and 980 nm, respectively.

Recently, $CaSc_2O_4$ and $SrSc_2O_4$ as hosts have attracted great interest for the design of new phosphors. Yb^{3+} doped Ca- and $SrSc_2O_4$ were investigated as potential solid state laser materials [24]. A novel Ce^{3+} doped $CaSc_2O_4$ phosphor was developed by Shimomura et al. which shows efficient green luminescence under excitation with blue LEDs [25]. Hao et al. reported on a tunable full-color emission of $CaSc_2O_4$:Eu^{3+} upon excitation at 395 nm [26], whereas the work of Müller et al. demonstrated that Eu^{2+} doped $SrSc_2O_4$ exhibits deep red persistent luminescence upon excitation at 525 nm [27].

To the best of our knowledge, there are no reports on the photoluminescence properties of Cr^{3+} doped (Sr,Ca)-scandates, which are, however, suitable host matrices for the incorporation of trivalent chromium ions in weak field octahedral sites. Herein, we will report on the broad band emission spectra of Cr^{3+} in $SrSc_2O_4$ and the influence of the Ca^{2+} substitution on the luminescence properties with regard to the crystal field strength and Racah parameters. Additionally, thermal quenching measurements were performed in order to examine the thermal stability of the broad band Cr^{3+} luminescence in view of their potential application as broad near infrared emitters for NIR pc-LEDs.

2. Experimental section

2.1. Synthesis

The phosphors $(Sr_{1-x}Ca_x)Sc_2O_4$:1%Cr^{3+} (x = 0, 0.2, 0.4, 0.6, 0.8, 1.0) were synthesized by solid state reaction in an ambient atmosphere of nitrogen. As starting materials $SrCO_3$ (Treibacher Industrie AG, 99.99%), $CaCO_3$ (Alfa Aesar, 99.95%), Sc_2O_3 (Treibacher Industrie AG, 99.99%) and Cr_2O_3 (Alfa Aesar, 99.95%) were used. The starting materials were mixed and ground in an agate mortar. The blends of the powders were placed in Mo boats and calcined at high temperatures. In the case of the $CaSc_2O_4$:Cr^{3+} the calcination process was performed at 1600 °C for 3 h. The other phosphors (Sr,Ca)Sc_2O_4:Cr^{3+} were synthesized by calcination at 1400 °C for 12 h.

2.2. Characterization

The X-ray diffraction patterns were measured on a Rigaku MiniFlex II diffractometer. As a radiation source a copper X-ray tube with Cu Kα radiation (λ = 1.54 Å) was used. The samples were examined in the region of 2θ between 10° and 80° with a scanning rate 10° per min.

Excitation and emission spectra were recorded on an Edinburgh Instruments FSL 920 spectrometer equipped with a 450 W Xe arc lamp, mirror optics for powder samples and a cooled (20 °C) single-photon counting photomultiplier from Hamamatsu (R2658P), which is sufficiently sensitive up to 1010 nm. The correction file for the emission spectra was obtained from calibration with a tungsten incandescent lamp certified by NPL (National Physics Laboratory, UK). Diffuse reflection spectra were recorded on an Edinburgh Instruments FS900 spectrometer equipped with a 450 W Xe arc lamp and a cooled single-photon counting photomultiplier (Hamamatsu R928). $BaSO_4$ (Sigma-Aldrich, 99.99%) was used as a reflectance standard. For recording thermal quenching (TQ) curves a cryostat "MicrostatN" from Oxford Instruments was introduced in the above described spectrometer. Measurements were carried out from 77 to 500 K in 50 K steps. For recording excitation and emission spectra at 2.7 K a He-cryostat "Optistat AC-V 12" from Oxford Instruments was introduced in the above described spectrometer.

The decay curves were measured using an Edinburgh Instruments FLS920 fluorescence spectrometer with a photomultiplier from Hamamatsu H74422-40. The samples were excited with an Edinburgh EPL655 pulsed diode laser (65 ps pulse width). For recording the temperature dependent decay curves from 4 to 350 K, an Oxford Instruments liquid helium flow cryostat was used.

Table 1
Cell parameters, molar weight, density of $CaSc_2O_4$ and $SrSc_2O_4$ [28], and the average distances between central metal ion (Sc^{3+}) and ligands (O^{2-}) in the $CaSc_2O_4$ and $SrSc_2O_4$ compounds [29].

Lattice parameters	$CaSc_2O_4$	$SrSc_2O_4$
a [Å]	9.461	9.698
b [Å]	11.122	11.302
c [Å]	3.143	3.185
M [g/mol]	193.99	241.53
Density [g/cm^3]	3.90	4.56
Sc(1) - O distance [Å]	2.063	2.083
Sc(2) - O distance [Å]	2.122	2.162

3. Results and discussion

3.1. Description of the structure of $CaSc_2O_4$ and $SrSc_2O_4$

$CaSc_2O_4$ and $SrSc_2O_4$ crystallize in the same structure corresponding to the calcium ferrate(III)-type [$CaFe_2O_4$]. Both compounds belong thus to the orthorhombic crystal system with the space group *Pnam* [24]. The unit cell parameters of both orthorhombic cells are listed in Table 1.

The $CaSc_2O_4$ and $SrSc_2O_4$ structure comprises two octahedral ScO_6 moieties, which are connected via edge forming double octahedrons (Fig. 1). Moreover, four of the double octahedrons are linked through the corners resulting in a tunnel structure containing large trigonal prismatic cavities which can by occupied by the large Sr^{2+} or Ca^{2+} ions [30]. Because of the rigid octahedron network $(Sc_2O_4)^{2-}$, compounds with larger cations than Sr^{2+} do not crystallize in the [$CaFe_2O_4$] type structure. For instance, $BaSc_2O_4$ crystallize in the monoclinic system with a perovskite type structure [31,32].

In the $CaSc_2O_4$ and $SrSc_2O_4$ structures, two different Sc^{3+} sites may be distinguished. Both Sc(1) and Sc(2) are octahedrally surrounded by oxygen anions. The Ca^{2+} and Sr^{2+} ions occupying the trigonal prismatic cavities are coordinated by eight oxygen anions [33].

Because of high crystal field stabilization energy of Cr^{3+} ions in the octahedral coordination, we predict a chromium substitution on the Sc^{3+} sites. Additionally, the similarity of crystal ionic radii: Sc^{3+}(88.5 pm), Cr^{3+}(75.5 pm) and identical charges of both ions support our prediction [34]. The crystal ionic radii of Ca^{2+} and Sr^{2+} ions in 8-fold coordination are 126 pm and 140 pm, respectively. Hence, it is unlikely that trivalent chromium ions replace Ca^{2+} or Sr^{2+} due to the much larger difference in ionic radii and the difference in charge.

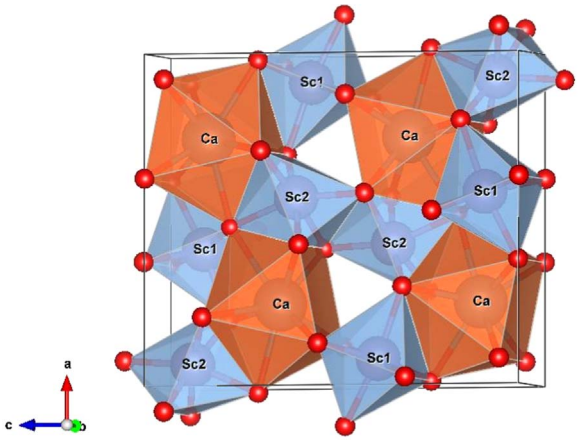

Fig. 1. The crystal structure of $CaSc_2O_4$.

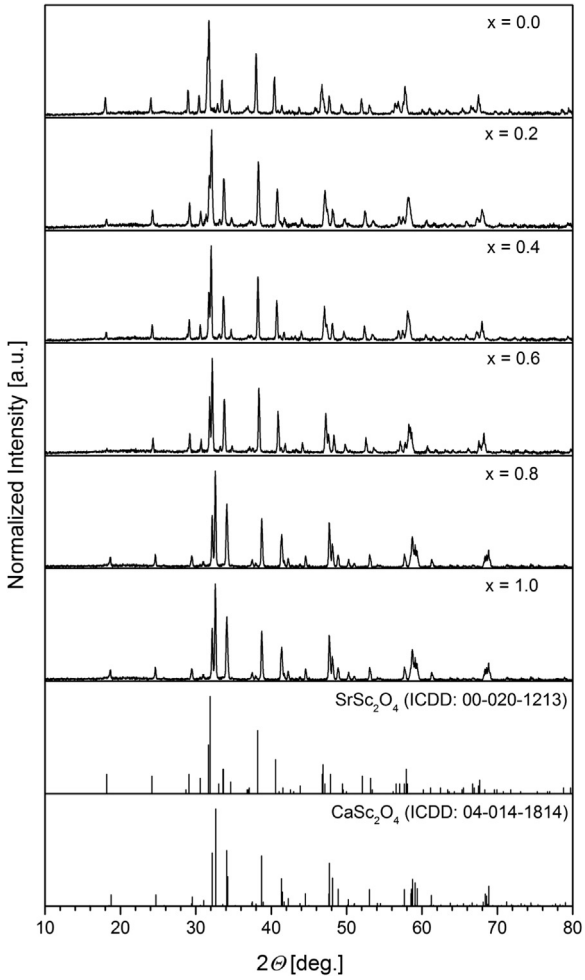

Fig. 2. XRD patterns of μ-scale powders of $(Sr_{1-x}Ca_x)Sc_2O_4$ doped with 1.0% of Cr^{3+} ions and ICDD reference data of $SrSc_2O_4$ and $CaSc_2O_4$.

In order to investigate the influence of the host material on the Cr^{3+} photoluminescence, it is necessary to consider the distances between Sc^{3+} metal ions and O^{2-} ligands. The value of the crystal field splitting is inversely proportional to the distance between cation and ligands (R) as given by the relation $10Dq \sim (1/R^5)$ [35]. It indicates that even a small change in the length of any metal–ligand bond considerably alters the crystal field splitting. By comparison the lengths of the Sc–O bonds in $SrSc_2O_4$ and $CaSc_2O_4$ structures (Table 1), we predict a larger splitting of the energy of the 3*d* orbitals for Cr^{3+} substitution on Sc^{3+} sites in $CaSc_2O_4$ in view of the smaller average Sc-O distances in $CaSc_2O_4$.

3.2. Phase formation

Crystal structure and phase purity of the $(Sr_{1-x}Ca_x)Sc_2O_4$:1.0%Cr^{3+} (x = 0, 0.2, 0.4, 0.6, 0.8, 1.0) phosphors were examined by recording X-ray diffraction patterns that are plotted in Fig. 2.

The $CaSc_2O_4$:Cr powder was synthesized at higher temperature (1600 °C/3 h) than (Sr,Ca)Sc_2O_4:Cr (1400 °C/12 h) because of the incomplete solid state reaction between raw materials at a lower temperature. It turns out that some Sc_2O_3 remains in the sample heated at 1400 °C what was also reported by Shimomura et al. [25]. In order to avoid the presence of unreacted Sc_2O_3 in the product, an excess of CaO was used to ensure complete reaction of Sc_2O_3 and the formation of single phase material [28].

In the case of $CaSc_2O_4$:Cr and $SrSc_2O_4$:Cr, the position and relative intensities of the observed XRD peaks are in good agreement with

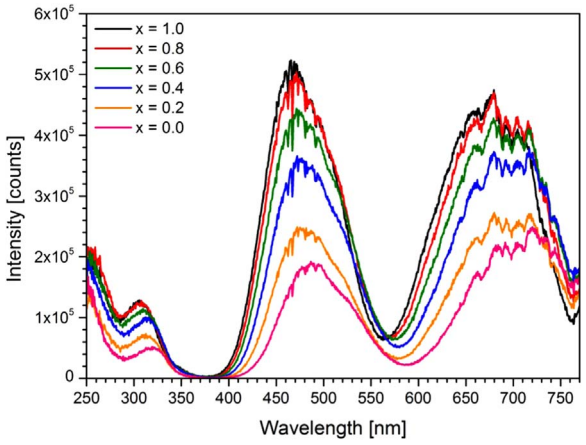

Fig. 3. Excitation spectra of $(Sr_{1-x}Ca_x)Sc_2O_4$ doped with 1.0% of Cr^{3+} recorded for 800 nm emission at room temperature. (Spectrometer alignment remained the same).

reference data (ICDD 04-014-1814 for $CaSc_2O_4$:Cr and ICDD 00-020-1213 for $SrSc_2O_4$:Cr). There is no evidence for the presence of impurity phases in the samples.

Replacing Sr^{2+} (ionic radii 140 pm) by Ca^{2+} (ionic radii 126 pm) in the analyzed scandates causes a considerably change of the diffraction peaks positions (Fig. 2). The increase of the concentration of the Ca^{2+} ions substituting for Sr^{2+} ions causes a shift of the XRD patterns to the higher diffraction angles. It indicates a decrease in the lattice constants due to the smaller ionic radius of Ca^{2+} in comparison to Sr^{2+}. In terms of Hume-Rothery rules i.e., the similarity of the ionic radius and electronegativity of both Ca^{2+} and Sr^{2+} ions, the same crystal structure and the same valence, we can conclude that the (Sr,Ca)Sc_2O_4:Cr compounds form a solid solution of two scandates [36].

3.3. Optical properties at room temperature

The excitation spectra of Cr^{3+}-doped $(Sr_{1-x}Ca_x)Sc_2O_4$ were monitored for a single emission wavelength (λ_{em} = 800 nm) at room temperature (RT) as displayed in Fig. 3. Three excitation bands located in the UV (near 300 nm), blue (near 470 nm) and deep red (near 680 nm) spectral range are observed. The excitation bands are attributed to the $^4A_2 \rightarrow {}^4T_1(^4P)$, $^4A_2 \rightarrow {}^4T_1(^4F)$ and $^4A_2 \rightarrow {}^4T_2(^4F)$ transitions of Cr^{3+}, respectively. A blue shift of the excitation spectra occurs, as the concentration of Ca^{2+} ions in $SrSc_2O_4$ increases. The excitation intensity gradually increases with increasing Ca concentration. The change in the excitation intensities can be explained by the difference in the emission intensity at 800 nm caused by a blue shift of the emission maximum with increasing Ca concentration (Fig. 4).

The photoluminescence spectra of Cr^{3+} in $(Sr_{1-x}Ca_x)Sc_2O_4$ recorded for the excitation at 470 nm are shown in Fig. 4. The dominant feature of the emission spectra is a broad band corresponding to the $^4T_2 \rightarrow {}^4A_2$ transition and extending from 700 nm to 1000 nm (or even longer wavelengths). The emission due to the $^2E \rightarrow {}^4A_2$ transition (R-lines) was not detected. A full width at half maximum (FWHM) at RT for all (Sr,Ca)-scandates is around 170 nm (2350 cm^{-1}). As in the case of the excitation spectra, the substitution of Ca^{2+} ions on Sr^{2+} sites causes a peak shift toward shorter wavelength. The emission spectrum of $CaSc_2O_4$:Cr (λ_{max} = 819 nm) is blue shifted for 650 cm^{-1} in comparison to the emission spectrum of $SrSc_2O_4$:Cr (λ_{max} = 860 nm).

As 3*d* electrons of the transition metal ions are not shielded from their surroundings by outer filled shells, the optical properties of Cr^{3+} are sensitive to the environment. The influence of the host lattice on the Cr^{3+} spectra is expressed by spectroscopic parameters such as the crystal field splitting (10*Dq*), and the *B* and *C* Racah parameters. In order to quantify the influence of the Ca^{2+} substitution for Sr^{2+} in the $SrSc_2O_4$, the values for 10*Dq*, *B* Racah parameter and *β*-covalency (B/B_0) were calculated from the energy maxima of the $^4A_2 \rightarrow {}^4T_2$ and

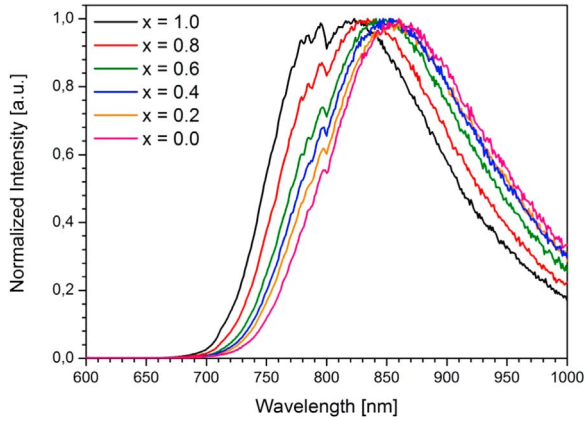

Fig. 4. Emission spectra of $(Sr_{1-x}Ca_x)Sc_2O_4$ doped with 1.0% of Cr^{3+} recorded for 470 nm excitation at room temperature.

Table 2
Crystal field splitting parameter 10*Dq*, *B* Racah parameters and *β*-covalency of Cr^{3+}-doped $(Sr_{1-x}Ca_x)Sc_2O_4$ as determined from the energy values at the maxima of the $^4A_2 \rightarrow {}^4T_2$ ($E(^4T_2)$) and $^4A_2 \rightarrow {}^4T_1$ ($E(^4T_1)$) absorption bands. B_0 is the free Cr^{3+} ion value and equals 918 cm^{-1} [38].

Parameter	E ($^4T_1$) [cm^{-1}]	E ($^4T_2$) [cm^{-1}]	*B* [cm^{-1}]	*Dq* [cm^{-1}]	10*Dq/B*	$\beta = B/B_0$
$SrSc_2O_4$	20,492	13,889	711	1389	19.5	0.7745
$Ca_{0.2}Sr_{0.8}Sc_2O_4$	20,747	14,124	708	1412	19.9	0.7712
$Ca_{0.4}Sr_{0.6}Sc_2O_4$	20,986	14,347	705	1435	20.3	0.7680
$Ca_{0.6}Sr_{0.4}Sc_2O_4$	21,097	14,450	703	1445	20.5	0.7658
$Ca_{0.8}Sr_{0.2}Sc_2O_4$	21,186	14,534	702	1453	20.7	0.7647
$CaSc_2O_4$	21,368	14,705	700	1471	21.0	0.7625

$^4A_2 \rightarrow {}^4T_1$ absorption bands and are collected in Table 2 [37].

The values of 10*Dq* for $SrSc_2O_4$ and $CaSc_2O_4$ are 13,889 cm^{-1} and 14,705 cm^{-1}, respectively. By comparing the values of the crystal field strength of (Sr,Ca)Sc_2O_4:Cr compounds (Table 2) with Al_2O_3:Cr (17,990 cm^{-1}, strong crystal field) [39], $YAl_3(BO_3)_4$:Cr (16,750 cm^{-1}, intermediate crystal field) [40], $LaSc_3(BO_3)_4$:Cr (15,290 cm^{-1}, weak crystal field) [41], we observe that the (Sr,Ca)-scandates belong to weak crystal field materials. In the Tanabe Sugano diagram (Fig. 5), the values of 10*Dq/B* for $CaSc_2O_4$:Cr (21.0) and for $SrSc_2O_4$:Cr (19.5) are indicated. The 10*Dq/B* value for $SrSc_2O_4$:Cr is located on the left side of the crossover line. With increasing Ca^{2+} concentration in $SrSc_2O_4$, the values of 10*Dq/B* increase. The 10*Dq/B* value for $CaSc_2O_4$ is 21.0 and according to the Tanabe Sugano diagram (Fig. 5), the $^4T_2$ level lies above the ^2E level.

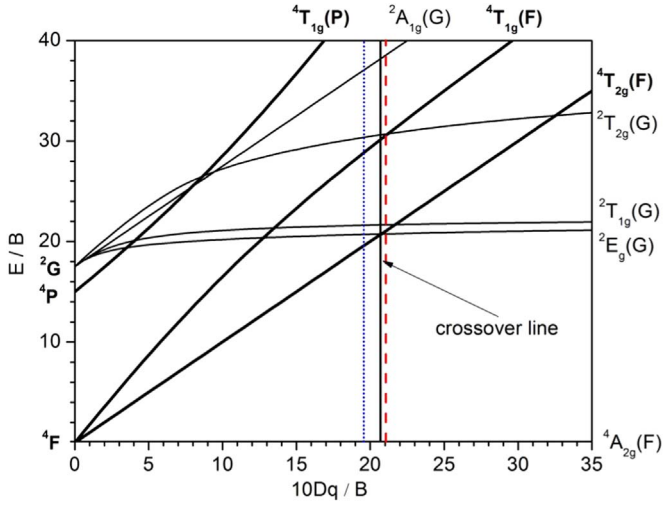

Fig. 5. Tanabe-Sugano diagram for the d^3 electronic configuration in octahedral symmetry. The 10*Dq/B* values of $SrSc_2O_4$:1%Cr (blue) and $CaSc_2O_4$:1%Cr (red) are indicated as vertical lines. (For interpretation of the references to color in this figure legend, the reader is referred to the web version of this article).

In the Tanabe Sugano diagram, the maxima of absorption bands of d^3-d^3 transitions determine the positions of the bands. According to the Franck-Condon principle, transitions from the ground state occur without change in the geometry of a molecule. Therefore, the ligand field strength does not change during the absorption process. For Cr^{3+}, the $^4A_2 \rightarrow {}^4T_2$ transition is expected to occur at the energy 10*Dq* – the energy separation between the t_2^3 ($^4A_2$) and t_2^2e ($^4T_2$) configuration in octahedral field. However, an accurate determination of the position of the electronic origin of the $^4T_2$ state in the given system is difficult and does not correspond with 10*Dq* as defined. Transitions take place to various vibrational levels of the excited state and the maximum of the absorption corresponds to a higher vibrational level [42]. In the emission spectrum of $CaSc_2O_4$:Cr recorded at room temperature (Fig. 4) and at 2.7 K (Fig. 8), the emission arising from the $^2E \rightarrow {}^4A_2$ transition is not observed. This shows that the zero vibrational level of the $^4T_2$ state is below the ^2E level and the Cr^{3+} ions occupy a weak crystal field site. In the low temperature emission spectra (vide infra) zero-phonon lines for the $^4T_2 \rightarrow {}^4A_2$ transition are observed around 750 nm which confirms that the electronic origin of the $^4T_2$ state is well below the ^2E state which is typically situated around 700 nm.

The ionic radii of Cr^{3+} and Sc^{3+} ions in octahedral coordination are 75.5 pm and 88.5 pm, respectively. According to the relation $10Dq \sim (1/R^5)$ [35], the crystal field strength is inversely proportional to the distance to the power of five of the metal ion to the centre of the ligand. The incorporation of Cr^{3+} ions onto the larger Sc^{3+} cation sites causes a considerably decrease of the crystal field strength. This explains that the energy of the $^4T_2$ state is lower than the energy of the ^2E state. As a result $^4T_2 \rightarrow {}^4A_2$ emission is observed which is a broad band emission in the NIR [43,44]. Increasing the concentration of Ca in $SrSc_2O_4$:Cr also results in a reduction of the *B* Racah parameters and indicates an increase of the covalent character of the Cr–O bonds. The higher covalency of the Cr^{3+}–O^{2-} bonds in the $CaSc_2O_4$ than in the $SrSc_2O_4$ host lattice is reflected by the reduced *β* value (0.7625 for $CaSc_2O_4$ and 0.7745 for $SrSc_2O_4$) (Fig. 6).

The 10*Dq* values show an increase with increasing Ca^{2+} concentration in $(Sr_{1-x}Ca_x)Sc_2O_4$ system, which is in line with the blue shift of excitation and emission bands upon Ca substitution. Moreover, according to the crystal field theory, decreasing lattice constants (Table 1) causes an increase of the crystal field strength and shifts the luminescence peaks towards shorter wavelengths. Nie et al. observed the same phenomenon in $CaAl_{12}O_{19}:Cr^{3+}$ and $SrAl_{12}O_{19}:Cr^{3+}$ [45]. The calculated crystal field strength for $CaAl_{12}O_{19}$:Cr (10*Dq* = 17360 cm^{-1}) is higher than for $SrAl_{12}O_{19}$:Cr (10*Dq* = 16970 cm^{-1}). The smaller value of

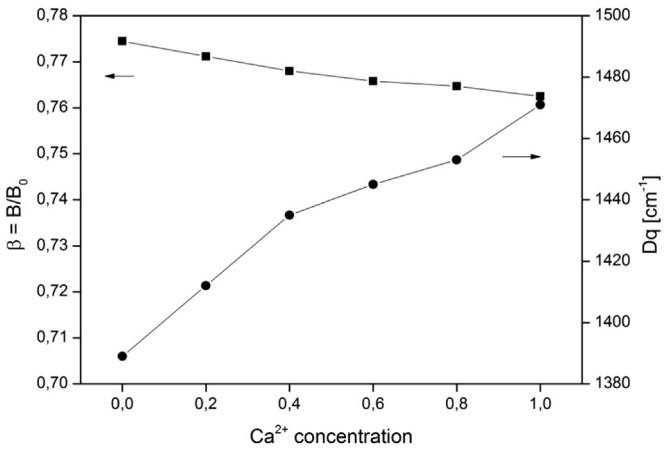

Fig. 6. Influence of the Ca-concentration on the crystal field strength (*Dq*) and *β*-covalency for Cr^{3+} in $(Sr_{1-x}Ca_x)Sc_2O_4$ (lines serve as a guide to the eye).

the B Racah parameter for Ca- aluminate ($B = 632\ cm^{-1}$) in comparison to Sr- aluminate ($B = 648\ cm^{-1}$) confirms the higher covalent character for the shorter Cr–O bonds.

The substitution of Ca^{2+} for Sr^{2+} in the structure causes a decrease of the lattice parameters as well as a shrinkage of the size of the MO_8 moiety, because of the smaller ionic radius of Ca^{2+} ion (126 pm) compared to Sr^{2+} ion (140 pm) [46]. Hence, the Sc–O distance in the ScO_6 octahedra decreases slightly as the Ca content increase. The average length of the Sc–O bonds in $CaSc_2O_4$ is 2.063 Å and 2.122 Å and in $SrSc_2O_4$ 2.083 Å and 2.162 Å, respectively, for the two Sc^{3+} sites in the two hosts (see Table 1). The longer the length of the metal to ligand bond, the smaller the crystal field splitting of the 3*d* level energy for Cr^{3+} substitution on Sc^{3+} sites in $SrSc_2O_4$ will be.

3.4. Temperature dependence of optical properties

To gain further insight in the luminescence properties of Cr^{3+} in the scandates, low temperature measurements were done. Measurements at cryogenic temperatures reveal spectral details that disappear at room temperature because of thermal broadening. In addition, temperature dependent emission spectra and luminescence decay measurements provide insight in thermal quenching of the emission. First we will discuss luminescence spectra recorded at 2.7 K. The excitation bands in the deep red range (580–750 nm) of Cr^{3+} doped (Sr,Ca)Sc_2O_4 recorded at room temperature display some features around 700 nm (see Fig. 3). To investigate the origin of these features high resolution excitation and emission spectra of $CaSc_2O_4$:Cr^{3+} and $SrSc_2O_4$:Cr^{3+} at 2.7 K were recorded and are displayed in Fig. 7 and Fig. 8, respectively. The excitation spectrum measured for 800 nm emission at 2.7 K shows more details and show different position of the peaks compared to the spectra recorded at RT. The three lowest energy excitation bands are assigned

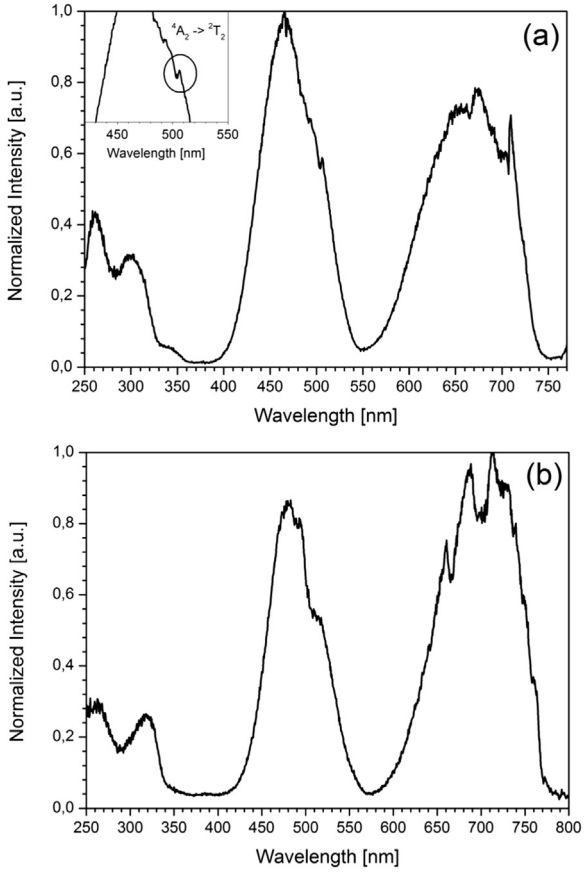

Fig. 7. Excitation spectra of $CaSc_2O_4$:1%Cr^{3+}(a) and $SrSc_2O_4$:1%Cr^{3+}(b) recorded at 2.7 K for emission at 800 nm and 870 nm, respectively.

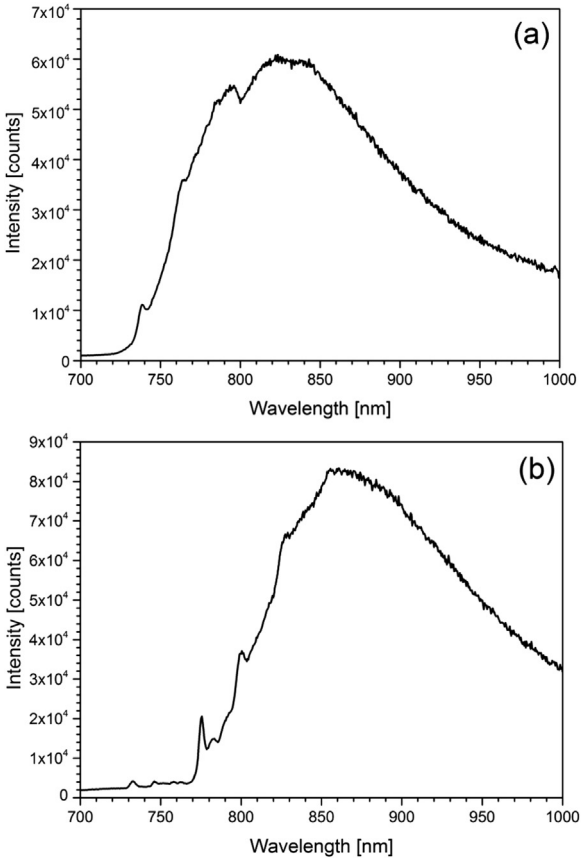

Fig. 8. Emission spectrum of $CaSc_2O_4$:1%Cr^{3+}(a) and $SrSc_2O_4$:1%Cr^{3+}(b) recorded at 2.7 K upon excitation at 470 nm and 480 nm, respectively.

to the three spin-allowed d-d transitions $^4A_2 \rightarrow {}^4T_2$ (~650–750 nm), $^4A_2 \rightarrow {}^4T_1$ (^4F) (~400–550 nm) and $^4A_2 \rightarrow {}^4T_1$ (^4P) (~280–330 nm). At shorter wavelengths a fourth band can now be clearly observed. The band gap of $CaSc_2O_4$ was determined to be 5.8 eV [47]. Therefore, the bands in the UV region cannot be ascribed to the host lattice absorption but rather to the O^{2-}–Cr^{3+} charge transfer. The maximum of the CT bands at 2.7 K in $CaSc_2O_4$:Cr and $SrSc_2O_4$:Cr appear at around 261 nm (38,314 cm^{-1}) and at 259 nm (38,610 cm^{-1}), respectively. A slightly lower energy charge transfer in $CaSc_2O_4$:Cr indicates a shorter Sc–O distance in $CaSc_2O_4$ compared to $SrSc_2O_4$. The shorter the distance between metal ion and ligands, the lower energy is required for a promotion of an electron from the oxygen orbital to the empty levels of the metal cation.

By comparison the excitation spectra recorded at RT (Fig. 3) to the spectra recorded at 2.7 K (Fig. 7), a blue shift of the charge transfer band (CT) with increasing temperature can be observed. A higher temperature causes an increase in vibrations in the crystal lattice of the host material. This extends the length of the bonds between metal and ligands and shifts the charge transfer band to higher energies at room temperature than at 2.7 K [48].

In the excitation spectrum of $CaSc_2O_4$:Cr recorded at 2.7 K (Fig. 7a) a sharp feature around 508 nm is just resolved (see inset Fig. 7(a)). On the low energy excitation bands in $CaSc_2O_4$:Cr and $SrSc_2O_4$:Cr two dips at around 665 nm (15,038 cm^{-1}) and 700 nm (14,286 cm^{-1}) are present. The spectral position of these dips coincides with the spectral position of the spin-forbidden transitions to the $^2T_2$ (~508 nm), $^2T_1$ (~665 nm) and ^2E (~700 nm) levels. Similar features have been observed before and assigned to Fano type interactions between the doublet states and the continuum of quartet states. Therefore, we can assign the features to Fano antiresonance arising from interaction between intraconfigurational $^2T_2$ and $^4T_1$ levels (~508 nm) and $^2T_1$ and ^2E levels and the $^4T_2$ level (665 and 700 nm) [49–52]. The effect of the orbital mixing

between the excited states by spin-orbit interaction is most pronounced in the systems showing excited state crossover ($10Dq/B \sim 21$), like in the case of the $LiCaAlF_6:Cr^{3+}$ [53], $Sc_2(WO_4)_3:Cr^{3+}$ [49], $Sc_2(MoO_4)_3:Cr^{3+}$ [54] and $MgMoO_4:Cr^{3+}$ [55].

Fig. 8 shows the emission spectra of Cr^{3+}-doped $CaSc_2O_4$ and $SrSc_2O_4$ monitored at 2.7 K upon excitation at 470 nm and 480 nm, respectively. The broad band NIR emission is assigned to the $^4T_2 \rightarrow {}^4A_2$ transition. The low temperature emission spectra reveal fine structure that is not clearly observed at 300 K. The observation of broad emission at 2.7 K confirms that the $^4T_2$ state is situated below the ^2E state and is the lowest excited state for Cr^{3+} in the two scandates.

The FWHM of the emission bands of $SrSc_2O_4$ and $CaSc_2O_4$ is 2050 cm^{-1} and 2405 cm^{-1}, respectively. The narrower emission band for Cr^{3+} in $SrSc_2O_4$ indicates that the electron-phonon coupling is weaker for the $^4T_2 \rightarrow {}^4A_2$ transition in $SrSc_2O_4$. The weaker electron-phonon coupling is also evident from the better resolved vibrational fine structure for the Cr^{3+} emission spectrum in $SrSc_2O_4:Cr^{3+}$ (Fig. 8b). The broad band emission spectrum of $CaSc_2O_4$ (Fig. 8a) displays two narrow peaks at 738 nm and 763 nm whereas the emission spectrum of $SrSc_2O_4$ (Fig. 8b) shows three narrow peaks at 775 nm, 800 nm and 827 nm. The narrow lines at 738 nm ($CaSc_2O_4$) and at 775 nm ($SrSc_2O_4$) can correspond to the $^4T_2 \rightarrow {}^4A_2$ zero-phonon line transition whereas the peaks at longer wavelengths can be assigned to the phonon satellites of the zero-phonon lines. From the relative intensities of the zero-phonon lines the Huang-Rhys parameters S were determined for $SrSc_2O_4$:Cr ($S = 4.7$) and $CaSc_2O_4$:Cr ($S = 5.3$) confirming the smaller electron-phonon coupling for the $^4T_2 \rightarrow {}^4A_2$ transition in $SrSc_2O_4:Cr^{3+}$. Yamaga et al. reported on the same phenomenon in Cr^{3+} doped $ZnWO_4$ [56]. They observed zero-phonon line of the $^4T_2 \rightarrow {}^4A_2$ transition and its phonon satellites at 826 nm and 870 nm, respectively. The energy difference between the zero-phonon line and phonon satellites were determined to be 440 cm^{-1} for $CaSc_2O_4$:Cr and 400 cm^{-1} for $SrSc_2O_4$:Cr and these differences reflect the energy of vibrational modes that couple with the $^4T_2 \rightarrow {}^4A_2$ transition.

In the $SrSc_2O_4$ and $CaSc_2O_4$ structures, based on the presence of two different Sc^{3+} sites, there are two different crystallographic Cr^{3+} sites. Nonetheless, in the emission spectrum recorded at low temperature (Fig. 8) only one zero-phonon line is observed. The absence of a second zero phonon line can be due to the overlap of the two inhomogeneously broadened zero-phonon lines. Alternatively, as the Huang-Rhys factor is rather high and only a weak zero-phonon line is observed, the Cr^{3+} emission for the second site may have a higher Huang-Rhys factor which prevents the observation of a zero-phonon line.

The emission spectrum of $SrSc_2O_4$ recorded at 2.7 K (Fig. 8b) reveals also a sharp peak at around 733 nm. A similar narrow line positioned at 734 nm has been reported e.g. in $LaAlO_3:Cr^{3+}$ and attributed to the $^2E \rightarrow {}^4A_2$ transition [57]. The crystal field for Cr^{3+} in $LaAlO_3$ is much stronger ($Dq = 1790$ cm^{-1}) than in $SrSc_2O_4$ ($Dq = 1389$ cm^{-1}). The ^2E level lies below $^4T_2$ level and the luminescence from this level dominates at room temperature. In the case of $SrSc_2O_4$, the quartet level has lower energy than the doublet level and the ^2E luminescence is not expected to be observed at 2.7 K as fast relaxation on a ps time scale is expected to the zero-vibrational level of the $^4T_2$ state. Still it is interesting to calculate the energy at which the ^2E state is expected in $SrSc_2O_4$. Assuming that the ratio of C and B Racah parameters for the ions of the first transition series is four ($C/B \approx 4$), the energy of the ^2E level can be estimated from the following equation $E(^2E) = 3.05C + 7.9B - 1.8B^2/Dq$ [37,58]. It turned out, that the energy of the ^2E level is 13,635 cm^{-1} (733.4 nm) and the peak with maximum at 733 nm can correspond to a $^2E \rightarrow {}^4A_2$ transition. The energy of the ^2E level is higher than the energy of the zero-phonon line of the $^4T_2$ emission and the difference energy ($E(^4T_2) - E(^2E)$) is -740 cm^{-1}. This makes it unlikely that the 733 nm emission is from Cr^{3+} on the Sc^{3+} site in $SrSc_2O_4$ but possibly there is a very small amount of an impurity phase, below the XRD detection limit, in which Cr^{3+} is incorporated and gives rise to ^2E emission at 733 nm.

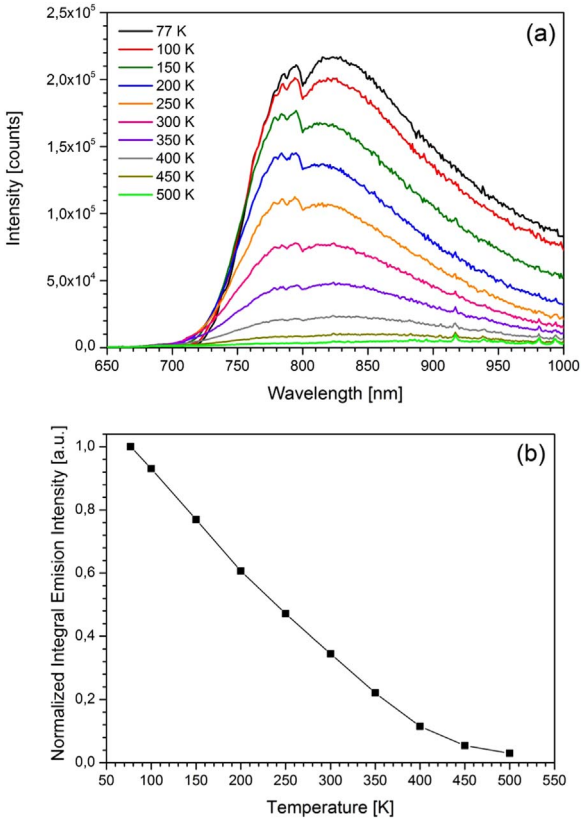

Fig. 9. Temperature dependent emission spectra (a) of $CaSc_2O_4$:1%Cr upon excitation at 470 nm and normalized integral emission intensity (b) as a function of the temperature of $CaSc_2O_4$:1%Cr.

To investigate the thermal quenching behavior of the emission temperature dependent emission spectra were recorded and also temperature dependent lifetime measurements were performed. The temperature dependence of the emission intensity was recorded under identical alignment conditions between 77 and 500 K. Fig. 9a displays the temperature dependent emission spectra of $CaSc_2O_4$:1%Cr^{3+}. At lower temperatures the emission spectra show only broad bands due to the $^4T_2 \rightarrow {}^4A_2$ transition. A characteristic dip at around 780 nm was identified to originate from the correction file in the NIR spectral range. The position of the emission bands for $CaSc_2O_4:Cr^{3+}$ and $SrSc_2O_4:Cr^{3+}$ shows a weak temperature dependence. The emission spectrum of $SrSc_2O_4$:Cr at 500 K is red shifted by about 250 cm^{-1} compared to the spectrum recorded at 77 K.

Fig. 9b displays the normalized integral emission intensity as a function of the temperature between 77 and 500 K. The thermal quenching of the Cr^{3+} luminescence already starts at 77 K. The broad band emission of $CaSc_2O_4$:Cr at room temperature is quite weak. At around 240 K, the intensity has decreased to 50% of the 77 K value.

To further investigate the thermal quenching behavior, luminescence lifetimes of the Cr^{3+} emission were recorded as a function of temperature between 4 and 350 K. Fig. 10 displays the temperature dependence of the decay time of the $^4T_2$ emission of Cr^{3+} ions in $CaSc_2O_4$ and $SrSc_2O_4$. All decay curves were recorded for the emission at 780 nm and 790 nm, respectively, upon pulsed (65 ps) excitation at 655 nm. The decay curves were fitted with bi-exponential function $I(t) = A_1\exp(-t/\tau_1) + A_2\exp(-t/\tau_2)$, where $I(t)$ is intensity at a given time t, A_1 and A_2 are constants, and τ_1 and τ_2 are the partial lifetimes for the exponential components. The bi-exponential fits can be explained by the two distinct crystallographic sites for Cr^{3+} in the $(Sr,Ca)Sc_2O_4$ structure.

At low temperatures a µs decay time is observed, which is typical for the spin-allowed but parity forbidden $^4T_2 \rightarrow {}^4A_2$ emission of Cr^{3+}

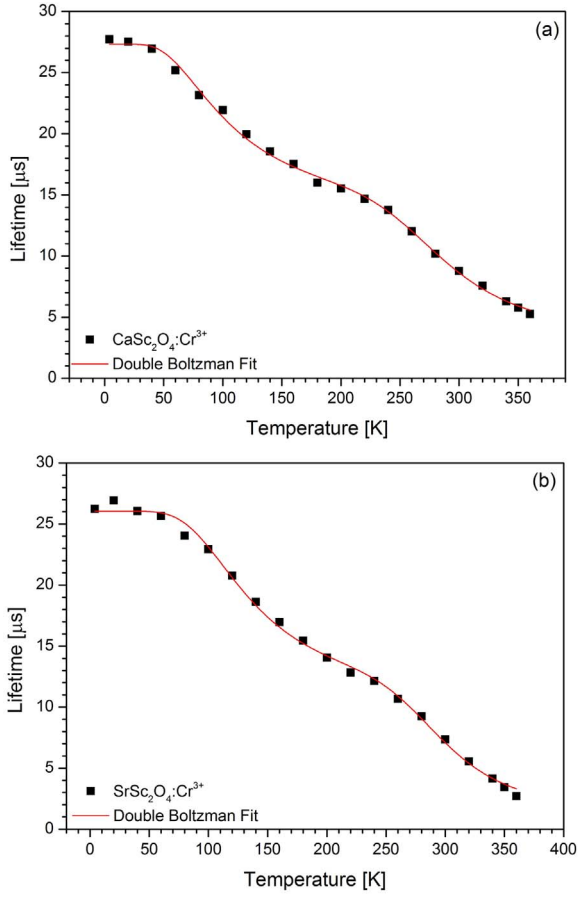

Fig. 10. Temperature dependent lifetime of the Cr^{3+} broad band emission ($^4T_2 \rightarrow {}^4A_2$) in $CaSc_2O_4$:Cr (a) and $SrSc_2O_4$:Cr (b) determined from bi-exponential fits of decay curves. The decay curves were recorded for the 780 nm and 790 nm emission under excitation at 655 nm for $CaSc_2O_4$:Cr and $SrSc_2O_4$:Cr, respectively.

[59,60]. The average decay times of the Cr^{3+} broad band emission in $CaSc_2O_4$ and $SrSc_2O_4$ at 4 K are similar to each other, viz. 27.6 µs and 26.2 µs. As already mentioned, the Cr^{3+} ion occupies crystallographic sites with a weak crystal field in $(Sr,Ca)Sc_2O_4$ and thus the lowest excited state is $^4T_2$. The ^2E state is hardly populated for excited Cr^{3+} ions and has a negligible impact on the emission lifetime. Hence, the decay time of $(Sr,Ca)Sc_2O_4$:Cr is mostly determined by radiative and non-radiative processes of the $^4T_2 \rightarrow {}^4A_2$ transition [61]. The decrease in decay time with temperature above ~70 K reflects that non-radiative processes set in and cause quenching of the $^4T_2$ emission. This observation is consistent with decrease in emission intensity above 77 K (Fig. 9).

The temperature dependence of the luminescence decay time does not show a monotonous decrease. Two stages can be discerned, one between 50 and 150 K and one between 200 and 350 K. We tentatively assign the two thermal quenching stages to Cr^{3+} on the two different crystallographic sites, but further research needs to be conducted to confirm this. To determine the quenching temperature (T_{50}, the temperature when the phosphor loses 50% of its efficiency) a double Boltzmann-sigmoidal function $\tau(T) = A\tau_{o,a}/(1 + B_a e^{(-Ea/kT)}) + (1-A)\tau_{o,b}/(1 + B_b e^{(-Eb/kT)})$ was used, where $\tau(T)$ is the average decay time at a certain temperature, A describes the fraction of the first term, $\tau_{o,a}$ and $\tau_{o,b}$ are the decay times at zero Kelvin, B_a and B_b are the quenching frequency factors, E_a and E_b are activation energies for thermal quenching, T is the temperature and k is the Boltzmann constant. The quenching temperatures were calculated based on the $T_{50} = -E_{a(b)}/\ln(1/B_{a(b)})$ equation. Two T_{50} values were obtained for each sample: $T_{50(a)} = 134$ K and $T_{50(b)} = 288$ K for $CaSc_2O_4$:Cr and $T_{50(a)} = 146$ K and $T_{50(b)} = 298$ K for $SrSc_2O_4$:Cr. The bi-sigmoidal behavior is explained by a different quenching behavior for the two different Cr^{3+} sites in $(Sr,Ca)Sc_2O_4$. In both materials, the Sc(2)–O distance is larger compared to the Sc(1)–O distance (Table 1). It can be expected that a faster nonradiative decay rate occurs for Cr^{3+} ions which occupy more larger Sc(2) sites in the host lattice. Accordingly, the larger metal-ligand distance, the smaller T_{50} values can be observed [62]. Hence, the higher $T_{50(a)}$ values are attributed to the Cr^{3+} ions on smaller Sc(1) sites and the lower $T_{50(b)}$ values to the Cr^{3+} ions on larger Sc(2) sites.

The quenching temperature of the Cr^{3+} luminescence in strontium and calcium scandates is much lower than in $YAl_3(BO_3)_4$ (640 K) [40]. The difference in the quenching temperature can be explained by comparing the values of the Stokes shift and the position of the emission band. In general, a larger Stokes shift and a lower energy position of the excited state results in a lower quenching temperatures [63]. The Stokes shifts were determined from the luminescence spectra recorded at 2.7 K. The Stokes shifts of the Cr^{3+} emission in $CaSc_2O_4$:Cr and $SrSc_2O_4$:Cr are 3042 cm^{-1} and 2939 cm^{-1}, respectively, while the Stokes shift in YAB:Cr was found to be 2862 cm^{-1} [40]. The crystal field splitting parameters for Sr,Ca-scandates ($10Dq$ for $CaSc_2O_4$:Cr = 14,710 cm^{-1}, $10Dq$ for $SrSc_2O_4$:Cr = 13,890 cm^{-1}) are much lower than for YAB:Cr ($10Dq$ = 16,750 cm^{-1}) which shifts the $^4T_2$ emission band to lower energies in the scandates. The combined effect of a larger Stokes shift and a lower energy $^4T_2$ level can explain the low quenching temperature of the $^4T_2$ emission of Cr^{3+} in the scandates. Based on the present observations it is evident that it will be difficult to realize efficient 750–1000 nm emission from Cr^{3+} at elevated temperatures. The low energy position of the $^4T_2$ level requires a very small Stokes shift to realize a high quenching temperature. Given the extremely high temperatures that are reached on chip (~150 °C) it may not be possible to obtain an efficient broad band 700–1000 nm emitting LED based on a NIR emitting phosphor on the blue LED.

4. Conclusions

The photoluminescence of Cr^{3+} in $(Sr_{1-x}Ca_x)Sc_2O_4$ was investigated for the first time. The synthesized compositions show broad band near infrared emission with a FWHM of about 2000–3000 cm^{-1}. This broad band emission is ascribed to the $^4T_2 \rightarrow {}^4A_2$ transition and is characteristic of Cr^{3+} in a low crystal field environment. The luminescence properties of $SrSc_2O_4$:Cr can be tuned by substitution of Ca^{2+} ions for Sr^{2+}. The emission spectrum of $CaSc_2O_4$:Cr (λ_{max} = 819 nm) in comparison to the $SrSc_2O_4$:Cr (λ_{max} = 860 nm) is blue shifted by about 650 cm^{-1}. Temperature dependent decay time measurements indicate that Cr^{3+} ions occupy two different Sc^{3+} sites in $(Sr,Ca)Sc_2O_4$. At low temperatures, a ~25 µs decay time is observed, typical of Cr^{3+} broad band $^4T_2$ emission. Temperature dependent measurements between 4 K and 500 K for $CaSc_2O_4$:Cr and $SrSc_2O_4$:Cr show low quenching temperatures for the broad band Cr^{3+} emission. Therefore, Cr^{3+} activated $(Sr,Ca)Sc_2O_4$ µ-scale powders will not be suitable for phosphor converted NIR LEDs. This study can be used as an inspiration for further optimization of novel NIR emitting materials for solid state light sources based on (In,Ga)N semiconductor LEDs. The main challenge will be minimizing the Stokes shift which is crucial in obtaining an efficient broad band NIR emitter.

Acknowledgements

We gratefully acknowledge financial support from the Merz Pharmaceuticals GmbH, Frankfurt am Main, Germany.

References

[1] T.H. Maiman, R.H. Hoskins, I.J. D'Haenens, C.K. Asawa, V. Evtuhov, Phys. Rev. 123 (1961) 1151.
[2] M. Yu Sharonov, A.B. Bykov, P. Rojas, V. Petricevic, R.R. Alfano, Phys. Rev. B 72 (2005) 115111.

[3] J.C. Walling, O.G. Peterson, H.P. Jennsen, R.C. Morris, E.W. O'Dell, IEEE J. Quantum Electron. QE-16 (1980) 1302.
[4] Z. Pan, Y.-Y. Lu, F. Liu, Nat. Mater. 11 (2012) 58.
[5] B. Atakan, C. Eckert, C. Pflitisch, Meas. Sci. Technol. 20 (2009) 075304.
[6] Z.Y. Zhang, K.T.V. Grattan, A.W. Palmer, Phys. Rev. B 51 (1995) 2656.
[7] N. Basavaraju, S. Sharma, A. Bessière, B. Viana, D. Gourier, K.R. Priolkar, J. Phys. D: Appl. Phys. 46 (2013) 375401.
[8] A. Bessière, S. Jacquart, K. Priolkar, A. Lecointre, B. Viana, D. Gourier, Opt. Express 19 (2011) 10131.
[9] A. Zabiliūtė-Karaliūnė, H. Dapkus, R.P. Petrauskas, S. Butkutė, A. Žukauskas, A. Kareiva, Lith. J. Phys. 55 (2015) 200.
[10] B. Malysa, T. Jüstel, D. Uhlich, I. Becker, H. Bettentrup, Infrared LED, DE102014107321 A1, 2015.
[11] C.-F. Lin, Y.-S. Su, B.-R. Wu, IEEE Photonics Technol. Lett. 14 (2002) 3.
[12] P.A. Martin, Chem. Soc. Rev. 31 (2002) 201.
[13] A. Godavarty, A.B. Thompson, R. Roy, M. Gurfinkel, M.J. Eppstein, C. Zhang, E.M. Sevick-Muraca, J. Biomed. Opt. 9 (2004) 488.
[14] M. Blanco, I. Villarroya, Trends Anal. Chem. 21 (2002) 240.
[15] P.K. Min, B.L. Goo, Laser Ther. 22 (2013) 43.
[16] R. Usamentiaga, P. Venegas, J. Guerediaga, L. Vega, J. Molleda, F.G. Bulnes, Sensors 14 (2014) 12305.
[17] C.B. Han, C. He, X.J. Li, Adv. Mater. 23 (2011) 4811.
[18] A. Lakshmanan, Luminescence and Display Phosphors: Phenomena and Applications, Nova Science Publishers, New York, 2008.
[19] T.H. Maiman, R.H. Hoskins, I.J. D'Haenens, C.K. Asawa, V. Evtuhov, Phys. Rev. 123 (1961) 1151.
[20] V. Singh, R.P.S. Chakradhar, J.L. Rao, J.-J. Zhu, Mater. Chem. Phys. 111 (2008) 143.
[21] N. Fuhrmann, T. Kissel, A. Dreizler, J. Brübach, Meas. Sci. Technol. 22 (2011) 045301.
[22] X. Long, Z. Lin, Z. Hu, G. Wang, T.P.J. Han, J. Alloy. Compd. 347 (2002) 52.
[23] K. PeterMann, G. Huber, J. Lumin. 31 & 32 (1984) 71.
[24] R. Gaume, B. Viana, J. Derouet, D. Vivien, Opt. Mater. 22 (2003) 107.
[25] Y. Shimomura, T. Kurushima, N. Kijima, J. Electrochem. Soc. 154 (2007) J234.
[26] Z. Hao, J. Zhang, X. Zhang, X. Wang, Opt. Mater. 33 (2011) 355.
[27] M. Müller, M. Volhard, T. Jüstel, RSC Adv. 6 (2016) 483.
[28] J.R. Carter, R.S. Feigelson, J. Am. Chem. Soc. 47 (1964) 141.
[29] M.R. Gaume, University Pierre and Marie Curie (Ph.D. thesis), Paris, 2002.
[30] Hk Müller-Buschbaum, J. Alloy. Compd. 349 (2003) 49.
[31] R.C. Ropp, Encyclopedia of The Alkaline Earth Compounds, Elsevier, Amsterdam, 2013.
[32] V. Agafonov, A. Kahn, D. Michel, M. Guymont, Mater. Res. Bull. 18 (1983) 975.
[33] Hk Müller-Buschbaum, H.G. Schnering, Z. Anorg. Allg. Chem. 336 (1965) 295.
[34] R.D. Shannon, Acta Cryst. A32 (1976) 751.
[35] R.G. Burns, Mineralogical Applications of Crystal Field Theory, 2nd ed., Cambridge University Press, Cambridge, 1993.
[36] R. Abbaschian, L. Abbaschian, R.E. Reed-Hill, Physical Metallurgy Principles, 4th ed., Cengage Learning, Stamford, 2009.
[37] B. Henderson, G.F. Imbusch, Optical Spectroscopy of Inorganic Crystals, Oxford University Press, Oxford, 1989.
[38] P.H.M. Uylings, A.J.J. Raassen, J.F. Wyart, J. Phys. B 17 (1984) 4103.
[39] C.P. Poole, J. Phys. Chem. Solids 25 (1964) 1169.
[40] B. Malysa, A. Meijerink, T. Jüstel, J. Lumin. 171 (2016) 246.
[41] X. Long, Z. Lin, Z. Hu, G. Wang, T.P.J. Han, J. Alloy. Compd. 347 (2002) 52.
[42] R.F. Gould, Advances in Chemistry Series, American Chemical Society Publications, Washington, 1967.
[43] A. Ikesue, Y.L. Aung, V. Lupei, Ceramic Lasers, Cambridge University Press, Cambridge, 2013.
[44] M. Yamaga, B. Henderson, K.P. O'Donnell, J. Phys. Condens. Matter 1 (1989) 9175.
[45] Z. Nie, J. Zhang, X. Zhang, X. Ren, W. Di, G. Zhang, D. Zhang, X.-J. Wang, J. Phys.: Condens. Matter 19 (2007) 076204.
[46] A.K. Prodjosantoso, B.J. Kennedy, B.A. Hunter, Cem. Concr. Res. 32 (2002) 647–655.
[47] J.P. Hilden, Fiber Crystal Growth of Cerium Doped Calcium Scandate, Strontium Yttrium Oxide, and Tristrontium Silicate (Ph.D. thesis), Technischen Universität Berlin, Berlin, 2013.
[48] M.N. Taran, K. Langer, A.N. Platonov, V.V. Indutny, Phys. Chem. Miner. 21 (1994) 360.
[49] K. Petermann, P. Mitzscherlich, IEEE J. Quant. Electron. QE-23 (1987) 1122.
[50] K. Hermanowicz, J. Phys.: Condens. Matter 18 (2006) 10601.
[51] A. Lempicki, L. Andrews, S.J. Nettel, B.C. McCollum, Phys. Rev. Lett. 44 (1980) 1234.
[52] O. Maalej, O. Taktak, B. Boulard, S. Kammoun, J. Phys. Chem. B 120 (2016) 7538.
[53] M.N. Sanz-Ortiz, F. Rodriguez, I. Hernandez, R. Valiente, S. Kück, Phys. Rev. B 81 (2010) 045114.
[54] G. Wang, Z. Lin, L. Zhang, Y. Huang, G. Wang, J. Lumin. 129 (2009) 1398.
[55] E. Cavalli, A. Belletti, M.G. Brik, J. Phys. Chem. Solids 69 (2008) 29.
[56] M. Yamaga, A. Marshall, K.P. O'Donnell, B. Henderson, J. Lumin. 47 (1990) 65.
[57] Y. Katayama, H. Kobayashi, S. Tanabe, Appl. Phys. Express 8 (2015) 012102.
[58] B.W. Pfennig, Principles of Inorganic Chemistry, John Wiley & Sons, New Jersey, 2015.
[59] G. Huber, J. Lumin. 39 (1988) 259.
[60] M. Grinberg, I. Jaskólska, S. Kück, W. Jaskólski, Phys. Rev. B 60 (1999) 959.
[61] Z. Zhang, K.T.V. Grattan, A.W. Palmer, Phys. Rev. B 48 (1993) 7772.
[62] F. Baur, T. Jüstel, J. Lumin. 177 (2016) 354.
[63] G.F. Imbusch, T.J. Glynn, G.P. Morgan, J. Lumin. 45 (1990) 63.